Urban Climate 67 (2026) 102978

Contents lists available at ScienceDirect

Urban Climate

journal homepage: www.elsevier.com/locate/uclim

# A mesoscale CFD framework for extreme temperature mapping in urban environments☆

Alessia Piazza [a,b,*], Girma T. Bitsuamlak [b], Maria Pia Repetto [a], Josip Žužul [a], Massimiliano Burlando [a]

[a] Department of Civil, Chemical and Environmental Engineering (DICCA), University of Genoa, Via Montallegro 1, 16145 Genoa, Italy
[b] WindEEE Research Facility/Department of Civil and Environmental Engineering, Western University, London, ON N6A 5B9, Canada

ARTICLE INFO

*Keywords:*
CFD
RANS
Urban microclimate
Heatwaves
Urban Heat Island (UHI) effect

ABSTRACT

This study presents a combined statistical and numerical framework for mapping extreme temperatures in a complex urban environment. The municipality of Genoa, a coastal city in Italy, was used as a case-study example. Historical temperature data from 14 meteorological stations were analyzed using the Generalized Extreme Value (GEV) distribution to establish a robust statistical characterization of extreme temperatures across the region. A detailed three-dimensional model of the city, incorporating topographic and land-cover information, was developed for conducting Computational Fluid Dynamics (CFD) simulations using OpenFOAM. Steady-state Reynolds-Averaged Navier-Stokes (RANS) simulations were performed to reproduce the thermal conditions associated with extreme summer and winter events. The simulated temperature fields were validated against observations from the weather stations, showing good overall agreement. The resulting datasets were used to generate high-resolution maps of extreme maximum and minimum temperatures, highlighting the spatial variability temperatures within the city, that is seen to be locally affected by terrain features like topography and texture. The proposed methodology demonstrates the potential of integrating statistical extreme value analysis with CFD modeling to support evidence-based urban planning and the development of targeted extreme temperature mitigation and adaptation strategies, also in the context of climate change, in complex urban environments.

## 1. Introduction

Since the prehistoric era, most of the global population has lived in small rural communities. However, over the past centuries, urbanization has driven a significant demographic shift: today, approximately half of the world's population (around 4 billion people) lives in urban areas (Ritchie et al., 2018). It is projected that 75% of the population will be living in cities by 2050 (Kadakia and Galea, 2023). Urban growth has led to increased demand for housing and infrastructures, resulting in urban sprawl and infill development (Korah et al., 2025). These changes have contributed to a rise in the use of impervious surfaces such as asphalt, buildings, and paved roads (Korah and Wimberly, 2024), which by modifying the local heat balance and contributing to greater heat absorption, augment the effect of extreme temperature events (Gohain et al., 2023) in cities.

☆ This article is part of a Special issue entitled: 'Urban Wind Environment' published in Urban Climate.

* Corresponding author at: Via Montallegro, 1, Genova 16145, Italy.
*E-mail address:* apiazz2@uwo.ca (A. Piazza).

https://doi.org/10.1016/j.uclim.2026.102978
Received 21 January 2026; Received in revised form 30 April 2026; Accepted 28 May 2026
Available online 11 June 2026
2212-0955/

Consequently, cities are now more vulnerable to the effects of climate change, particularly extreme heat events. These phenomena typically manifest in two forms: the Urban Heat Island (UHI) effect and heatwaves. The UHI effect occurs when the temperature in urban areas is higher than the surrounding rural zones (Voogt and Oke, 2003) due to the heat-absorbing and heat-releasing properties of impervious surfaces, as well as the increased release of anthropogenic heat (Oke, 1982; Stewart and Oke, 2012a). Heat waves, on the other hand, refer to prolonged periods of anomalously high temperatures (Schielicke and Pfahl, 2022) that can affect larger areas. These two phenomena often coincide, amplifying their individual effects and exacerbating urban temperatures from June to September in the northern hemisphere (Founda and Santamouris, 2017; Milner et al., 2017). According to the 2023 Intergovernmental Panel on Climate Change (IPCC) report, every additional 0.5 °C of global warming is expected to increase the intensity and frequency of heatwaves (IPCC, 2023).

The combined impact of UHI and heatwaves intensifies the heat stress, particularly among vulnerable individuals, such as elderlies, young children, people with chronic diseases, those experiencing homelessness and individuals living in socially deprived areas (Kong et al., 2021). Since 1950, wide areas across Europe have experienced intense and prolonged heatwaves (Russo et al., 2015). During the 2003 heat wave, temperatures reached exceptionally high anomalies and were directly associated with up to 70,000 excess deaths across Europe (Mitchell et al., 2016). In particular, this heatwave highlighted the failure of social and health systems to adequately respond to such extreme events (Garcia-Herrera et al., 2010), which are becoming increasingly frequent and intense. It is therefore vital to develop a framework for understanding and mitigating the impacts of urban heat hazards.

As suggested by Mirzaei and Haghighat (2010) and further elaborated by Toparlar et al. (2015), two primary approaches can be used to study the UHI effect and urban temperatures: observational and simulation-based methods. The observational approach relies on measurement techniques, including urban temperature monitoring, that can be conducted through various methods, such as weather stations (Luna et al., 2006), remote sensors (Voogt and Oke, 2003), mobile traverses (cars or people with sensors) (Pigliautile and Pisello, 2018) and satellite imagery (Yao et al., 2022). While weather stations and mobile traverses provide accurate data at the pedestrian level, they often cover limited areas and may not capture the full temperature distribution of an entire city, depending on many weather stations are located and the designed route for the mobile traverses (Romero Rodríguez et al., 2020). Satellite imagery, on the other hand, often suffers from low spatial resolution. For instance, Sentinel-3 (ESA) offers a spatial resolution of 1 km and a temporal resolution of 1 day (Andriambololonaharisoamalala et al., 2025). In addition to spatial constraints, temporal aspects must also be considered. Observational approaches, such as weather monitoring stations, provide reliable information on past and present conditions, whereas simulation approaches, such as Computational Fluid Dynamics (CFD), can also explore potential future scenarios. CFD has recently gained traction for analyzing heatwaves and urban microclimates, offering detailed insight into temperature and flow distributions within complex urban settings (De Quadros et al., 2024; Kim and Lee, 2024; Toparlar et al., 2015). While CFD provides a powerful tool to explore temperature distribution, its application at the city scale remains challenging due to the increased computational demand caused by the modeling complexity of heterogeneous urban environments. Nevertheless, as the availability of High-Performance Computing (HPC) resources continue to grow and more efficient modeling frameworks are developed, city-scale simulations are becoming increasingly feasible. These developments provide an opportunity to conduct high-fidelity, multi-physics CFD simulations at large scale, enabling the generation of high-resolution maps of urban extreme temperatures that can play a key role in guiding resilient urban planning and public health decision making. By quantifying temperature variations across a city, heat-vulnerable areas can be identified, enabling city planners to develop targeted and efficient risk management strategies.

While numerous studies have examined the temperature distribution in cities through satellite imagery or simplified empirical models, no studies to best of authors' knowledge have combined in-situ meteorological data with high-resolution CFD simulations across an entire urban area. The integration of these approaches provides a unique opportunity to produce realistic, spatially detailed, and physically consistent temperature maps that can support evidence-based climate adaptation strategies.

The objective of this study is to develop high-resolution maps of extreme temperatures using CFD simulations aimed at reproducing high-resolution urban temperature distributions. For this, an open-source CFD solver, OpenFOAM, is used to carry out steady-state simulations of temperature variations across an entire city for extreme thermal events of different intensities, corresponding to return periods of 5 and 50 years. Two sets of simulations are conducted for each return period, one representing summer conditions (maximum temperatures), and the other representing winter conditions (minimum temperatures). The results of the simulations are compared with the extreme values obtained from the statistical analysis of the measurements coming from several weather stations located across the entire city which provided target conditions and consequently produced the heat maps. The use of an open-source platform enhances the transparency, reproducibility and accessibility of the modeling framework, promoting a broader adoption of CFD tools in urban climate modeling. The main objective of this paper is therefore to establish a proof-of-concept framework for generating mesoscale extreme temperature maps by integrating CFD simulations with long-term observations from meteorological stations.

## 2. Case study and full-scale data description

### 2.1. Case study

The Municipality of Genoa, which is a part of the Liguria region and located in the north-western part of Italy, is selected as the case study. In Europe, coastal cities like Genoa are witnessing more frequent storms, floods, heatwaves and droughts (Laino and Iglesias, 2023). While flooding is a well-known issue for the city of Genoa and has been extensively studied (Buzzi et al., 2014; Cassola et al., 2016), extreme heat is becoming an increasing concern. According to Masselot et al. (2025), Genoa is among the cities in the southern region of Europe where even a modest increase in temperature can dramatically increase the excess death rate. These characteristics make Genoa an ideal representative case for studying urban heat distribution and for testing mitigation strategies that could inform resilient urban planning in similar Mediterranean cities.

### 2.2. Description of full-scale data

Within the city and its surroundings, several meteorological stations belonging to the Regional Agency for Environmental Protection of Liguria (ARPAL) have been selected and used for the statistical characterization of the temperature (Fig. 1). The selected stations are representative meteorological stations with medium-to long-term observation datasets, with a sufficient duration to carry out an extreme value analysis of the temperature. These stations are equipped with instruments that can record wind speed (at a subset of stations), pressure, temperature and humidity (PTH), with wind measurements acquired at 10 m above ground and PTH measurements at 2 m above ground. The PTH instrumentation is shielded to prevent direct sunlight from affecting the thermometers and to protect the hygrometers from wind, ensuring reliable and accurate measurements. A summary of the stations is presented in Table 1.

The daily maximum temperature values were extracted from the time series recorded with an acquisition frequency of 30 min. The raw dataset has been checked to detect incorrect values, which were filtered out. Fig. 2, for illustrative purposes, shows the time series of the daily temperature maxima from 2004 to 2024 for a representative station (CFUNZ) located inside the urban area. The measurements corresponding to summer months (June to September), shown in red dots, were identified. It can be observed that, for this specific station, the maximum temperature never exceeds 40 °C, while the temperature minima do not fall below −5 °C.

Fig. 3a shows the daily temperature maxima of the same station presented in Fig. 2, with Gaussian mixture distribution model (GMModel) fitted to the data. This graph clearly exhibits a bi-modal distribution, reflecting seasonal variation. As presented, one peak occurs around 18 °C, corresponding to winter temperatures, while a second peak occurs around 29 °C, corresponding to summer temperatures, which are more relevant for extreme thermal events. Fig. 3b shows the daily temperature maxima limited to the summer months (Jun-Sep) and Fig. 3d limited to the winter months (Nov-Feb) with a Gaussian distribution superimposed.

A Generalized Extreme Value (GEV) distribution was fitted to the data to quantify uncertainty and derive confidence intervals for a given return period (Fig. 4). This approach has been widely used in literature (Aksu, 2021; Auld et al., 2023; Thompson et al., 2023) for both maximum and minimum temperature analyses. To determine the confidence interval of the GEV distribution, the three parameters- shape ($\xi$), scale ($\sigma$) and location ($\mu$)- were estimated from the original measurement dataset using the Maximum Likelihood Estimation (MLE) method. Since the shape parameter ($\xi$) controls tail behavior, values of $\xi > 0$ correspond to a type II (Fréchet) distribution. It has been demonstrated that for certain phenomena, such as wind speed, $\xi > 0$ can lead to physically unrealistic results (Holmes, 2007). This limitation was considered applicable to temperatures as well, and therefore $\xi$ was restricted to $\xi \leq 0$. This analysis was repeated for each meteorological station to obtain temperatures corresponding to various return periods. The resulting values for 5- and 50-year return periods for each station are summarized Table 2.

## 3. Methodology

### 3.1. Computational setup: domain, grid, and surface characterization

This section outlines the step-by-step procedure used to construct the domain, generate the computational mesh and define its structure, characteristics and refinement strategy. The computational domain is bounded by several patches, with each having a grid


**Fig. 1.** Aerial view of the Municipality of Genoa indicating the positions of the meteorological stations used in this study.

**Table 1**
Overview of the meteorological stations, indicating station code, altitude, duration of observations, and type of observations.

| Station code. | Altitude (m ASL) | Duration of observations | Observation* |
|---|---|---|---|
| CFUNZ | 30 | 03/06/2004-27/05/2024 | T, H |
| GEPTX | 75 | 01/01/2004–27/05/2024 | T |
| GEPEG | 69 | 01/01/2004–27/05/2024 | T |
| GEBOL | 47 | 01/01/2004–27/05/2024 | T |
| FIORI | 290 | 01/01/2004–27/05/2024 | T |
| RIGHI | 360 | 01/01/2004–27/05/2024 | T, W |
| GEQUE | 200 | 27/06/2013–27/05/2024 | T, H |
| STILA | 174 | 17/03/2010–27/05/2024 | T, H, W |
| MADGR | 104 | 01/01/2004–27/05/2024 | T, H |
| MOPEN | 980 | 23/05/2014–27/05/2024 | T, H, W |
| PREMA | 234 | 01/01/2004–27/05/2024 | T |
| MGAZZ | 310 | 01/01/2004–27/05/2024 | T |
| FFRES | 791 | 01/03/2001–27/05/2024 | T, W |
| PTURC | 590 | 01/01/2004–27/05/2024 | T, W |

* Temperature (T), Humidity (H), Wind speed and direction (W).

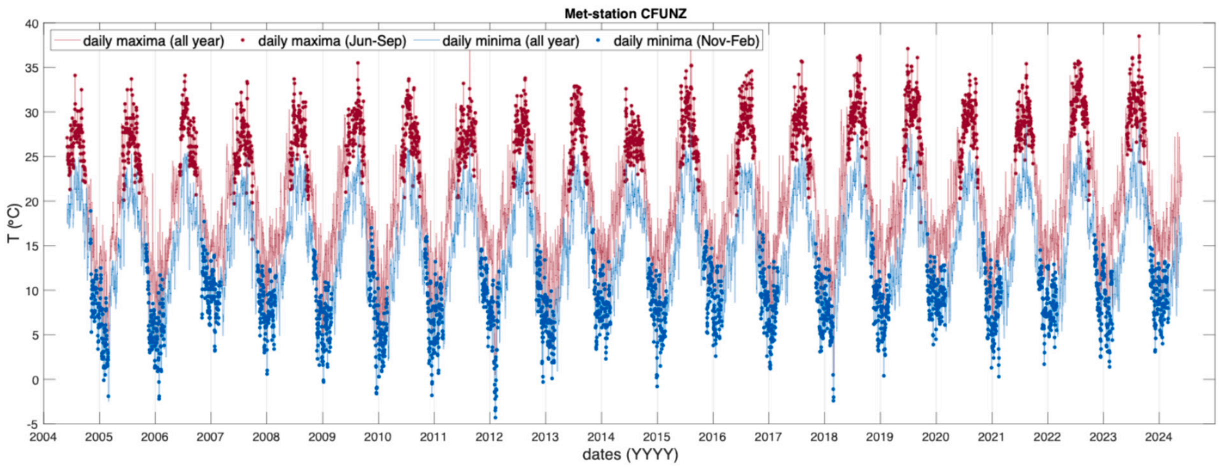


**Fig. 2.** Daily maximum and minimum temperatures recorded at CFUNZ over the full observation period.

resolution tailored to capture its specific flow characteristics. Higher grid resolution is applied in regions expected to experience greater turbulence to ensure more accurate representation of flow features. The terrain roughness is implicitly modeled by mapping the aerodynamic roughness length across the ground using a novel approach based on the CORINE land cover dataset, allowing for a more precise and standardized representation of surface heterogeneity across the domain.

### *3.1.1. Computational domain*

The computational domain covers an area of 40 km × 20 km × 3 km, which is considered big enough to include the whole urban area of the city of Genoa, along with a surrounding area of several kilometers that is expected to cover the overall circulation induced by the UHI. A schematic of the computation domain is presented in Fig. 5. During the warmest extreme events that occur in summer, anticyclonic conditions prevail (see for example Unger, 1996) that force very low-to-null surface winds, while the local circulation is expected to be mainly thermally induced by land-sea thermal contrasts and land cover type differences. Moreover, as found by Pongracz et al. (2006) and reported by Giannaros and Melas (2012), the UHI effect is exacerbated by anticyclone conditions, while under cyclonic conditions the UHI values decrease (e.g. Kassomenos and Katsoulis, 2006). This effect is related to the negative correlation between UHI and wind speed and cloud cover (Kim and Baik, 2005). The coldest winter events, instead, correspond to advective conditions (Ivajnšič and Žiberna, 2019) typically from the Siberian area. This meteorological situation, which is inducive of low surface wind conditions, can locally determine strong downslope winds in a few valleys around Genoa (Burlando et al., 2017), affecting limited portions of some urban neighborhoods. The flow within the domain is therefore, in both cases, driven primarily by surface heating/cooling and temperature differences, enabling the development of UHI-induced convective circulations. Accordingly, background winds with classical ABL inflow conditions are not imposed at the lateral boundaries of the computational domain, allowing the simulation to capture the development of local thermal/buoyancy-driven circulations relevant to extreme urban temperatures.

The computational domain is bounded by a total of 7 patches that represent the sides (North, South, East and West), top, ground and sea boundaries of the domain. The ground boundary is characterized by the type of terrain (urban and rural area, that includes the

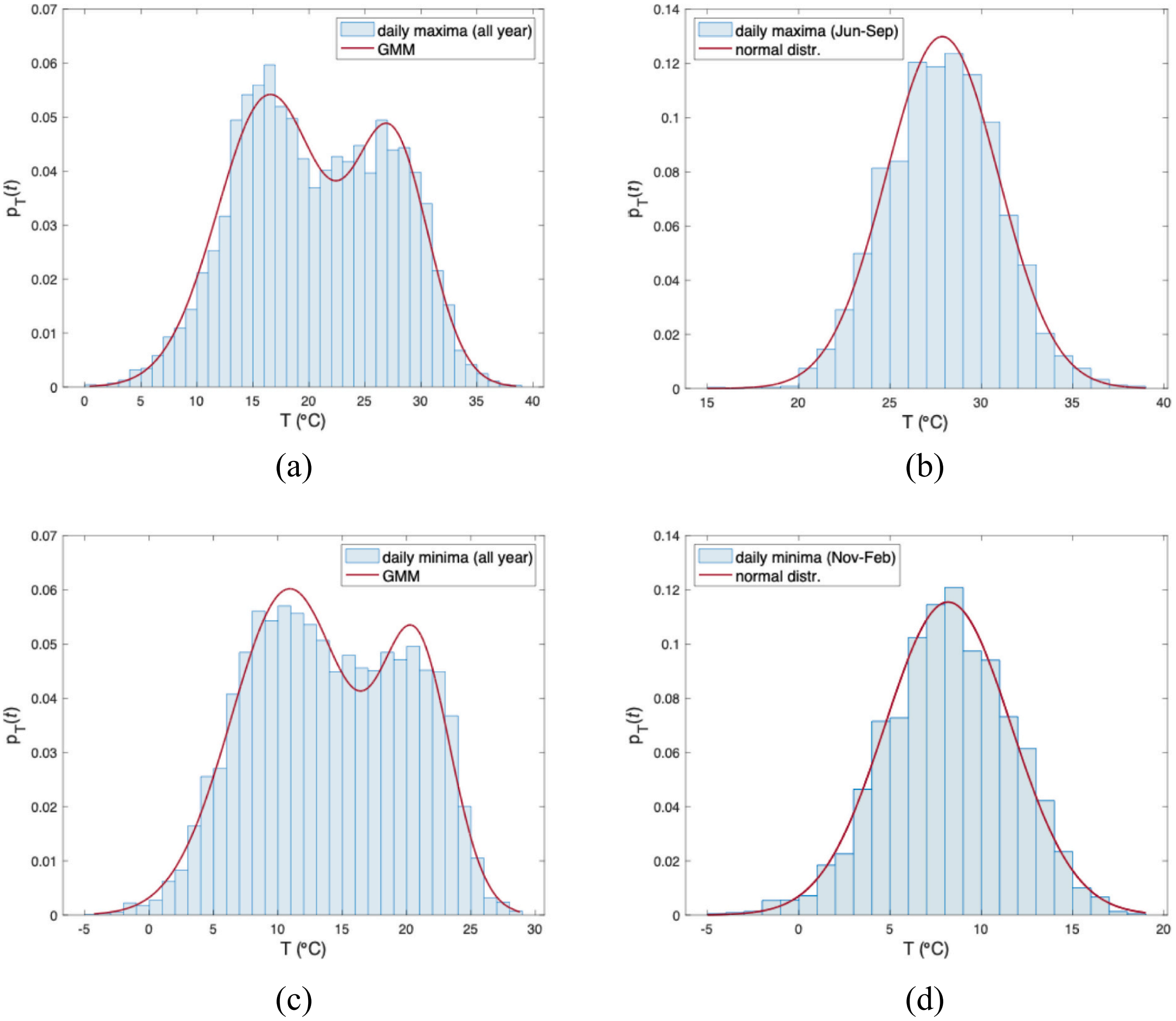


**Fig. 3.** Probability density functions for (a) daily maxima (all year), (b) daily maxima (Jun-Sept), (c) daily minima (all year) and (d) daily minima (Nov-Feb) for CFUNZ.

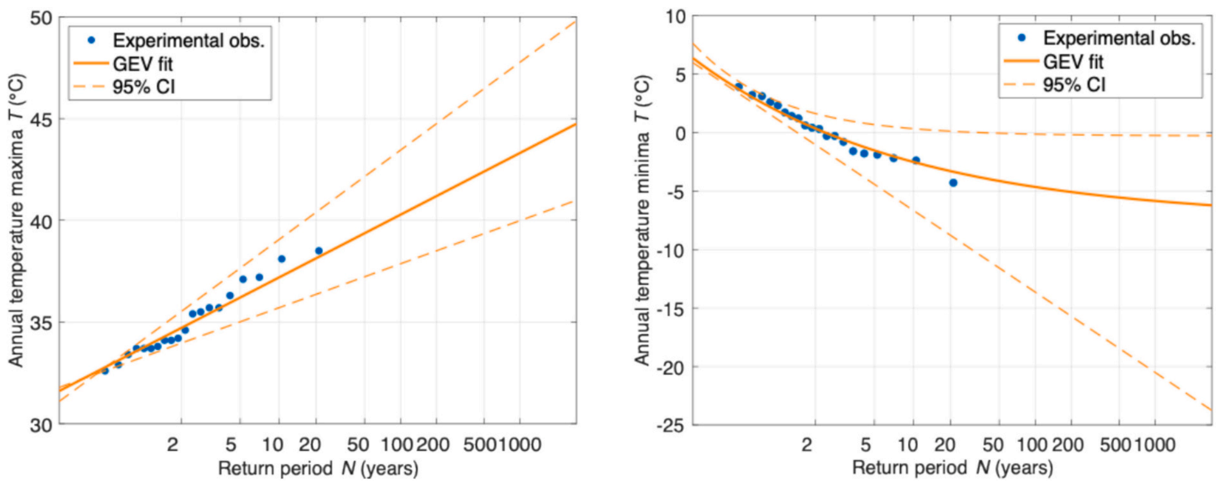


**Fig. 4.** Generalized Extreme Value (GEV) distribution applied on the measured yearly temperature maxima and minima for the CFUNZ dataset.

**Table 2**
Maximum and minimum temperature values for 5- and 50-year return periods estimated from GEV distribution.

| | T max (°C) | | | | | | | | | | | | | |
|---|---|---|---|---|---|---|---|---|---|---|---|---|---|---|
| Tr (years) | CFUNZ | GEPEG | GEBOL | GEPTX | FIORI | RIGHI | GEQUE | FFRES | MGAZZ | MADGR | PREMA | STILA | PTURC | MOPEN |
| 5 | 36.2 | 35.7 | 36.8 | 36.5 | 35.1 | 34.1 | 36.4 | 31.8 | 34.5 | 36.2 | 35.6 | 35.4 | 33.2 | 32.0 |
| 50 | 39.4 | 38.4 | 38.8 | 39.8 | 37.7 | 37.2 | 38.5 | 33.4 | 37.1 | 38.5 | 36.4 | 36.2 | 35.1 | 34.8 |
| | T min (°C) | | | | | | | | | | | | | |
| Tr (years) | CFUNZ | GEPEG | GEBOL | GEPTX | FIORI | RIGHI | GEQUE | FFRES | MGAZZ | MADGR | PREMA | STILA | PTURC | MOPEN |
| 5 | −1.5 | −2.3 | −2.7 | −4.2 | −3.5 | −4.3 | −1.3 | −6.7 | −3.3 | −3.2 | −3.8 | −1.1 | −9.0 | −8.6 |
| 50 | −4.1 | −5.4 | −5.7 | −6.9 | −6.6 | −8.1 | −4.7 | −9.2 | −6.4 | −6.4 | −7.3 | −6.0 | −12.4 | −12.8 |

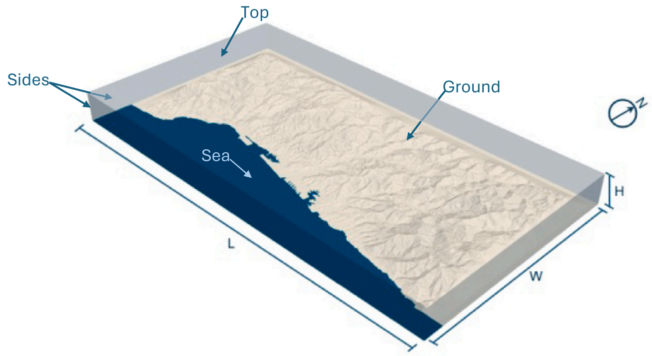


**Fig. 5.** Computational domain showing various control surfaces and overall dimensions.

hills around the city of Genova).

To ensure that the model accurately represents real-world conditions and is readily applicable for analysis, the computational domain was defined using the Universal Transverse Mercator (UTM) coordinate system. This allows precise georeferencing of the urban terrain and meteorological stations and ensures that the spatially varying simulation outputs can be directly mapped onto the actual city layout for subsequent analysis. The CFD best practice guidelines for pedestrian wind around buildings (Tominaga et al., 2008) recommends including some of the surroundings around the area of interest. The same principle was applied in this study, where additional area was modeled around the Municipality. As the topography of the terrain in the area is dominated by hills around the boundaries, a buffer region was additionally added to avoid any possible numerical stability issues caused by irregular boundaries (Žužul et al., 2025). Moreover, the domain height, set to 3 km, was chosen to be approximately three times greater than the maximum terrain elevation (~1000 m ASL) in order to minimize the potential boundary effects and prevent artificial flow acceleration. As mentioned in the introduction, the computational domain does not explicitly include the urban texture, which was implicitly modeled using techniques explained in Section 3.1.3.

### 3.1.2. Computational grid

CfMesh utility of the open source CFD software OpenFOAM was used to discretize the domain into predominantly hexahedral cells. Different mesh refinements levels were tested to achieve a balance between computational accuracy and computational feasibility.

Cell sizes of 20 m and 10 m in the horizontal direction were used for the sea and the terrain, respectively. Additional boundary layers for the terrain were used to ensure a finer refinement in the vertical direction close to the ground (Fig. 6). The need for a finer vertical refinement close to the ground is dictated by the temperature field that displays high gradients close to the ground and the fact that full-scale data from the meteorological stations used for model validation are available at 2 m height.

A grid independence study was carried out to ensure that the numerical results are not influenced by the discretization of the computational domain. Such a study is essential to verify that the solution accurately represents the physical phenomena rather than being affected by the mesh resolution. Four levels of mesh refinement, denoted as G0, G1, G2, and G3 were tested to assess the sensitivity of the solution to grid resolution. The details about these grid resolutions have been summarized in Table 3. The impact of mesh refinement was evaluated based on variations in the mean temperature and velocity fields across the domain.

Fig. 7 shows the mean temperature (T) and longitudinal velocity (U) profiles at the location of a representative meteorological station. The difference between the temperature and velocity profiles obtained from G2 and G3 mesh resolution becomes almost negligible. The marginal improvements in the results from G2 to G3 mesh demonstrate grid independence of the present setup. The G2 grid resolution was selected (H = 2 m) as it provided a sufficient level of accuracy, with further refinement yielding negligible improvements. It represents an optimal balance between computational efficiency and numerical accuracy.

### 3.1.3. CORINE land cover and terrain subdivision

The urban texture within the scope of this study as mentioned in the introduction has been implicitly modeled using the subdivision of the land obtained from CORINE Land Cover (CLC) dataset (Wyatt et al., 1988). CLC offers a pan-European land cover and land use

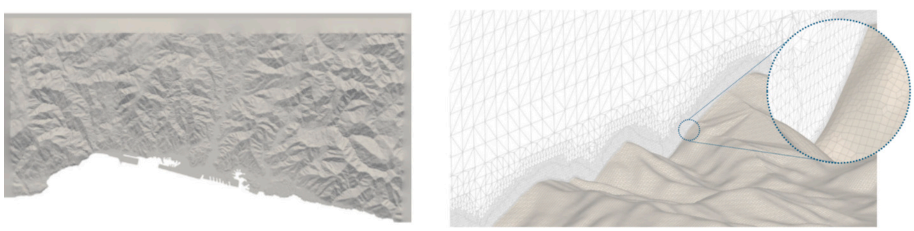

**Fig. 6.** Computational mesh showing cell distribution and refinement zones used in the simulations.

**Table 3**
Summary of the grid refinements employed in the grid independence study. The reference (i.e., at the ground) cell height is H = 10 m.

| Grid. | Cell size refinement in height | Total cell count |
|---|---|---|
| G0 | $H$ | ~ 70 M |
| G1 | $H/2$ | ~ 90 M |
| G2 | $H/5$ | ~ 108 M |
| G3 | $H/6.5$ | ~ 118 M |

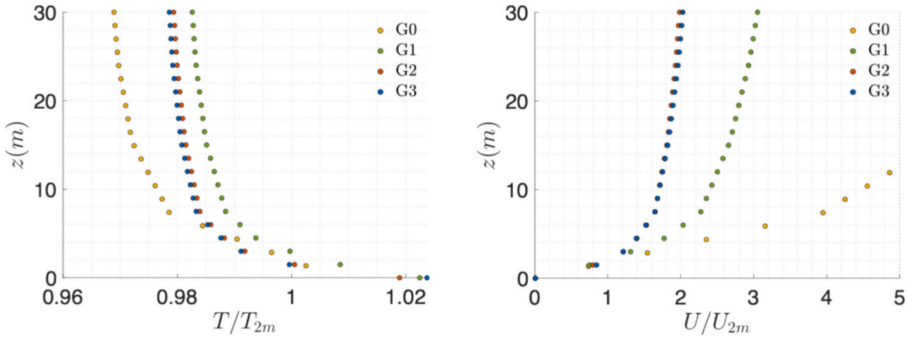


**Fig. 7.** Temperature and velocity profiles used to assess grid independence, showing negligible differences between successive mesh refinements (from G2 to G3).

inventory with 44 thematic classes, ranging from broad forested areas to individual vineyards. It is updated with new state-of-the-art and land cover layers every six years, with the most recent update made in 2018. This method, developed and firstly introduced by Ricci and Burlando (2025) allows the automation and standardization of terrain subdivision process, without the need to rely on manual visual inspection. The patch information is extracted for the entire Municipality of Genoa and elaborated using QGIS. Each patch is directly associated to a code depending on the land cover type and therefore to an aerodynamics roughness $z_{0.}$ For this research 22 different land covers have been identified and taken into consideration, as shown in Fig. 8. It is important to note that within the urban area identified by the CORINE land cover dataset, green areas or green infrastructures are largely absent, whereas the surrounding rural areas are almost entirely covered by vegetation.

The ground surface boundary (see Fig. 5) was therefore effectively replaced with 22 new patches, with each of them being representative of an area related to the specific roughness class determined by CLC. Having defined these new patches, the corresponding aerodynamic roughness lengths ($z_0$) were specified individually for each patch. The values of $z_0$ defined based on the Davenport classification (Davenport, 1961) and later updated by Wieringa (1992), range from $z_0 = 0.004$ m for the sea up to $z_0 = 0.8$ m for discontinuous urban fabric, increasing with the degree of urbanization. More detailed information about the roughness can be found in Table 4. An important consideration is the mesh resolution. Since the patches are applied directly to the mesh, the horizontal resolution must be sufficiently fine to avoid discontinuities at patch boundaries (Ricci and Burlando, 2025).

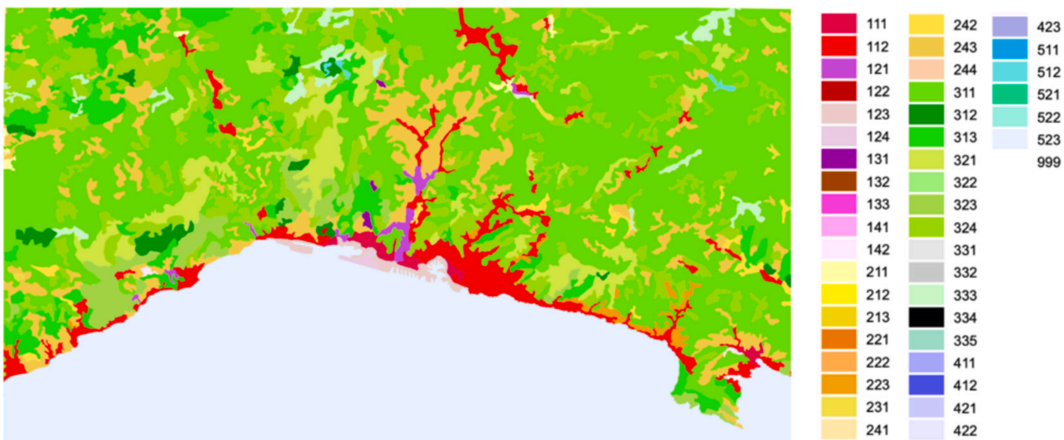


**Fig. 8.** CORINE Land Cover (CLC) contour identified for the area of Genoa.

### 3.2. Boundary conditions

This section provides the boundary conditions, and the numerical settings adopted for carrying out the CFD simulations. Four different simulations were performed to estimate the temperatures in the urban environment with boundary conditions corresponding to extreme events of varying risks of 5-, 50-year return periods.

The boundary conditions for different flow variables are summarized in Table 5 and Table 6. The computational domain is treated as a closed volume since, as explained in Section 3.1.1, the meteorological conditions corresponding to high (low) extreme temperatures in Genoa occur during anticyclonic (advective) conditions, and they both correspond to low surface wind conditions. This also allows to avoid numerical instabilities, with no inlet or outlet patches defined. It is important to highlight that, in these conditions, the flow is buoyancy-driven and is therefore generated internally because of temperature gradients and the resulting density differences. The UHI effect was therefore reproduced by considering only sensible heat flux and anthropogenic heat sources at the ground. Different heat flux values were applied to different patches in the urban area according to their specific land cover and land use characteristics. $z_0$ was used exclusively to characterize the aerodynamic roughness associated with each land-cover class and therefore to regulate near-surface momentum transfer. However, since roughness length primarily controls aerodynamic exchange rather than surface thermal behavior, thermal differentiation between surface types was introduced separately through spatially variable sensible heat flux boundary conditions. In this way, the thermal response of each surface category was represented through effective thermal forcing rather than solely through roughness length. Higher sensible heat flux values were assigned to dense residential and industrial zones, while lower values were prescribed for airport, port, and sparsely built-up areas. Because the simulations were performed under steady-state conditions, unresolved contributions such as thermal inertia, radiative exchange, and evapotranspiration were incorporated indirectly into the effective sensible heat flux imposed at the surface. The sensible heat flux measurement, defined as the covariance of the temperature and the vertical velocity component ($\overline{T'w'}$), is not straightforward and requires at least two high-precision thermometers to capture temperature gradient, but also two probes to measure the wind speed (and direction). Therefore, initial estimates for the heat fluxes in Mediterranean cities were derived from the literature. In particular, Mestayer et al. (2005) reported measurements of sensible heat flux in the city of Marseille (France) during summer days. These measurements were adopted as initial estimates for this study and subsequently adjusted, via trial-and-error, to account for the specific urban characteristics and climatic conditions of Genoa. Since cold waves are not a major concern in the Mediterranea area, it was more difficult to find initial estimates for the winter conditions, so a trial-and-error approach was used. The heat fluxes were iteratively adjusted within the literature-constrained interval until the simulated near-surface air temperatures at the reference monitoring locations reproduced the observed thermal range during the selected period. Although air temperature increases across return periods, the prescribed heat fluxes applied during the summer period were kept unchanged, since the dominant contributions to sensible heat flux are associated with longwave radiation and anthropogenic heat release. The differences among simulations of different return periods instead arise from the modified surrounding boundary conditions imposed on the rural area for each return period. The winter period presented a more complex scenario, as the flow was increasingly governed by localized effects. The anthropogenic heat was selected based on the guidelines of Local Climatic Zone (Stewart and Oke, 2012b). The selected final values for each simulation are therefore presented in Table 5.

For the heat fluxes, the temperature boundary condition atmTurbulentHeatFluxTemperature is used and is represented by the equation:

**Table 4**
CLC codes and land cover associated with different values of roughness length $z_0$.

| CLC code. | Typology of land cover | $z_0$ (m) |
|---|---|---|
| 111 | Continuous urban fabric | 0.7 |
| 112 | Discontinuous urban fabric | 0.8 |
| 121 | Industrial or commercial units | 0.55 |
| 123 | Port areas | 0.7 |
| 124 | Airports | 0.03 |
| 131 | Mineral extraction sites | 0.2 |
| 142 | Sport and leisure facility | 0.5 |
| 211 | Non-irrigated arable land | 0.1 |
| 223 | Olive groves | 0.25 |
| 231 | Pastures | 0.04 |
| 242 | Complex cultivation patterns | 0.1 |
| 243 | Land principally occupied by agriculture, with significant areas of natural vegetation | 0.25 |
| 311 | Broad-leaved forest | 0.6 |
| 321 | Coniferous forest | 0.6 |
| 313 | Mixed forest | 0.6 |
| 321 | Natural grasslands | 0.1 |
| 323 | Sclerophyllous vegetation | 0.2 |
| 324 | Transitional woodland-shrub | 0.2 |
| 331 | Beaches, dunes, sand | 0.003 |
| 333 | Sparsely vegetated areas | 0.1 |
| 512 | Water bodies | 0.0005 |
| 523 | Sea and Ocean | 0.004 |

**Table 5**
Input parameters applied to the main patches for each return period.

| Return period. | Heat flux Urban | Heat flux Industrial | Heat flux port | Heat flux airport | Temperature Lapse rate |
|---|---|---|---|---|---|
| Maximum temperature $T_r = 5$ years | 500 $W/m^2$ | 550 $W/m^2$ | 450 $W/m^2$ | 200 $W/m^2$ | 4 °C/km |
| Maximum temperature $T_r = 50$ years | 500 $W/m^2$ | 550 $W/m^2$ | 450 $W/m^2$ | 200 $W/m^2$ | 4.3°C/km |
| Minimum temperature Tr = 5 years | 550 $W/m^2$ | 400 $W/m^2$ | 450 $W/m^2$ | 200 $W/m^2$ | 11.7 °C/km |
| Minimum temperature Tr = 50 years | 450 $W/m^2$ | 350 $W/m^2$ | 450 $W/m^2$ | 200 $W/m^2$ | 9.7 °C/km |

**Table 6**
Summary of boundary conditions applied in the CFD simulations.

| | Fields | | | | | | |
|---|---|---|---|---|---|---|---|
| patch name | U | p_rgh | T | k | epsilon | nut | alphat |
| top | slip | 1 | fixedValue | zeroGradient | zeroGradient | zeroGradient | zeroGradient |
| sea | noSlip | 1 | fixedValue | kqRwallFunction | 2 | 3 | 4 |
| sides | slip | 1 | zeroGradient | zeroGradient | zeroGradient | zeroGradient | zeroGradient |
| Ground (urban) | noSlip | 1 | 5 | kqRwallFunction | 2 | 3 | 4 |
| Ground (rural) | noSlip | 1 | fixedValue | kqRwallFunction | 2 | 3 | 4 |

1. fixedFluxPressure 2. epsilonWallFunction 3.atmNutkWallFunction 4.atmAlphatkWallFunction 5.atmTurbulentHeatFluxTemperature

$$\nabla T = \frac{q}{C_p \alpha_p + \zeta} \tag{1}$$

where $\nabla T$ is the temperature gradient, $q$ is the heat flux, $C_p$ is the heat capacity of the fluid, $\alpha_p$ is the effective thermal diffusivity, that is estimated using the atmAlphatkWallFunction for the $\alpha'$ (turbulent thermal diffusivity) field, and $\zeta$ is a small value introduced to reduce numerical instabilities. The value of $\alpha'$ depends on the turbulent Prandtl number $Pr_t$ of the fluid and the roughness of the patch $z_0$ through the value of $E'$, defined as roughness-corrected dimensionless wall distance, and follows the temperature law-of-the wall as shown below:

$$\alpha' = \frac{u^* k y}{Pr_t \ln(\max(E', 1 + 10^{-4}))} + \frac{\nu_m}{Pr_t} \tag{2}$$

A fixed value of temperature was set for the rural areas, mainly characterized by olive groves, agricultural fields and forests. However, given the significant topographical variations within the rural domain, a spatially uniform temperature boundary condition would be inadequate as surface temperature varies with terrain elevation. To account for this, a temperature lapse rate is introduced to adjust the boundary condition with height. Consequently, a non-uniform Dirichlet boundary condition is adopted, where surface temperatures are adjusted locally to account for the temperature lapse rate across the varying terrain elevation. The temperature lapse rate is defined as:

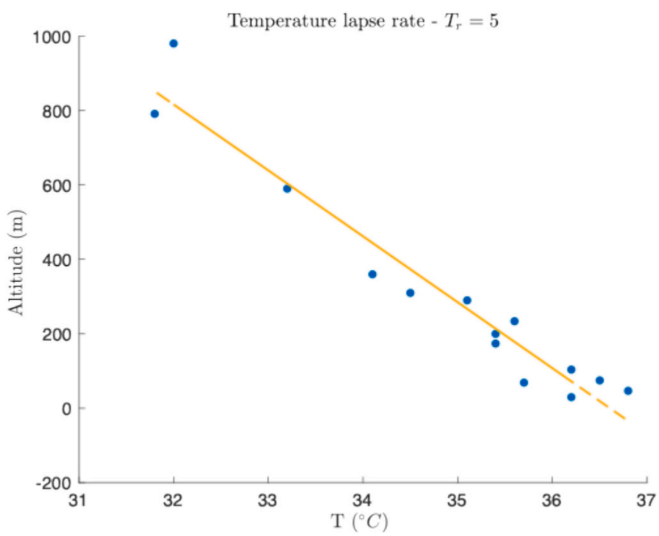


**Fig. 9.** Temperature variation with altitude for different weather stations for the 5-year return period maximum temperature case.

$$\Gamma = -\frac{dT}{dz} \tag{3}$$

where $T$ represents the temperature and $z$ the height above the sea level. It was estimated by plotting temperatures from different weather stations against their altitude (Fig. 9) for each return period and was assigned across the rural area.

The lapse rate was also used to estimate the temperature at the top boundary, which was set to constant value. Another key aspect is the selection of the wall function for the estimation of the $\nu_t$ parameter. As mentioned in Section 3.1.3, different values of roughness length ($z_0$) were assigned to every patch and specified in the atmNutkWallFunction dictionary. This wall function is based on the theoretical expression from Hargreaves and Wright (2007) and is based on the roughness length $z_0$ rather than the roughness height $k_s$, which is a more appropriate description of the roughness characteristics for the atmospheric boundary layer and coherent with the formulation of the law-of-the-wall commonly adopted in meteorology for ABL modeling. Table 6 presents a summary of the boundary conditions used for the simulations.

### 3.3. Turbulence modeling and solver settings

The CFD simulations were performed using the open-source software OpenFOAM/v2312, employing a 3D steady-state RANS solver utilizing the Boussinesq approximation to account for buoyancy effects. The standard $k-\varepsilon$ turbulence model was adopted for the present study. It is one of the most widely adopted approaches in CFD simulations of urban microclimates (Allegrini et al., 2015; Bouyer et al., 2011; Santiago et al., 2014), due to its robustness and relatively low computational cost. The turbulent kinetic energy $k$ and the turbulent dissipation rate $\varepsilon$ in this model are described by Richards and Hoxey (1993):

$$k = \frac{u^{*2}}{\sqrt{C_\mu}} \tag{4}$$

$$\varepsilon = \frac{u^{*3}}{\kappa(z + z_0)} \tag{5}$$

where $u^*$ is the friction velocity, $C_\mu$ is the model constant (0.09), $\kappa$ is the von Karman constant and $z_0$ is the aerodynamic roughness length. The SIMPLE algorithm was adopted to couple pressure and velocity fields. Numerical convergence was considered achieved when the residuals stabilized with no fluctuations and continued to only marginally decrease with further iterations. All the simulations were executed on an HPC system using a cluster with 256 cores and 4GB memory/core for each simulation for approximately 24–30 h. The solution was considered converged when the residuals drop below a threshold of $10^{-4}$ and remained stable. The details of the solvers, discretization schemes and other relevant parameters used for the study have been summarized in Table 7.

## 4. Results and discussion

This section presents the outcomes of the CFD simulations and the subsequent generation of extreme temperature maps for the Municipality of Genoa. The results are analyzed for multiple return periods, capturing the spatial variations in urban temperatures. Attention is given to the manifestation of the UHI effect, local hotspots, and the influence of topography and land cover on temperature distribution. Comparisons with observational data are provided where available to evaluate the accuracy of the simulations and the reliability of the generated heat maps. Two sets of simulations – one representing summer conditions (maximum temperatures) and the other representing winter conditions (minimum temperatures) were conducted for 2 return periods (5-year and 50-year), resulting in a total of four simulation cases.

**Table 7**
Description of the solvers, discretization schemes, turbulence model and fluid and transport properties.

| Item. | Description |
|---|---|
| Solver | BuoyantBoussinesqSimpleFoam<br>p_rgh: PCG with DIC<br>*U,T,k,* $\epsilon$: PBiCGStab with DILU |
| Discretization schemes | Temporal: steady<br>Gradient: Gauss linear<br>Divergence: bounded Gauss upwind<br>Laplacian: Gauss linear corrected<br>Interpolation: linear<br>Surface-normal gradient: corrected |
| Turbulence | RANS, $k-\epsilon$ |
| Fluid and transport properties | Kinematic viscosity, $\nu$ : 1e-05 $m^2s$<br>Laminar Prandtl Number, $Pr$: 0.7<br>Turbulent Prandtl Number, $Pr_t$: 0.85<br>Thermal expansion coefficient, $\beta$ : 3e-04 $K^{-1}$ |

(a)

(b)

(c)

(d)

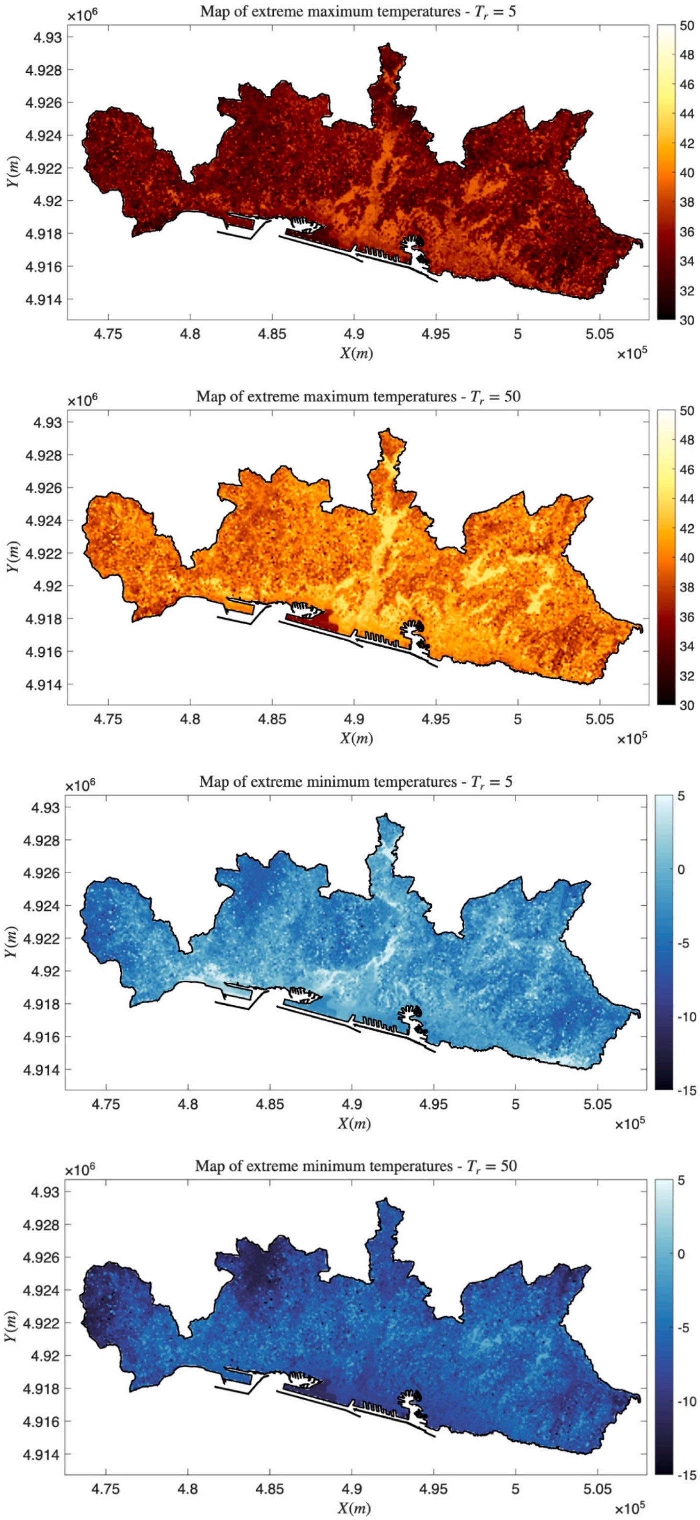


**Fig. 10.** Contour maps of extreme temperatures for (a) maximum temperatures (5-year return period), (b) maximum temperatures (50-year return period), (c) minimum temperatures (5-year return period), (d) minimum temperatures (50-year return period).

### 4.1. Maps of extreme temperature

To extrapolate the temperature at a height of 2 m and account for the underlying topography, the terrain in the STL format was first shifted along the z-axis by 2 m and then intersected with the simulation results using the surfaces post-processing function in OpenFOAM. This procedure allowed the extraction of temperature values at each point in the domain corresponding to the standard measurement height of 2 m above ground. To obtain the exact temperature at 2 m, linear interpolation was applied between the values at the first and second cell centroids. The results were eventually re-gridded onto a regular grid with a spatial resolution of 100 m × 100 m. As described in Section 3.1.1, some peripheral areas around the city were included in the computational domain to improve the accuracy of the simulations. For the purpose of generating maps specifically for the Municipality of Genoa, these extended areas were subsequently removed from the final contours presented in this section by intersecting the results with the municipal boundaries.

The extreme maximum and minimum temperature maps for return periods of 5 and 50 years, respectively, are presented in Fig. 10. For all the scenarios, the UHI effect is clearly visible, with urban areas (namely codes 111, 112, 121, 122, 123, and 124 of the CORINE Land Cover, see Fig. 8) exhibiting higher temperatures compared to the surrounding rural zones. However, this effect is less prominent in the winter conditions. This can be primarily attributed to the scarcity of vegetation and the prevalence of impervious surfaces within the city, whereas the surrounding countryside is largely covered by vegetation. In certain locations, elevated temperatures persist, a pattern consistent with the findings of Mei et al. (2025) who investigated the temperature distribution over complex terrain and reported that topographic complexity and surface heterogeneity can lead to localized thermal retention. Higher temperatures are observed both along ridges and at the bottom of valleys, with some thermal hotspots particularly evident in the east end of the region (right-hand portion of the figure). These localized peaks are likely caused by reduced ventilation due to the topography and may also reflect limitations in the use of CORINE land cover data: even when categorized under the same roughness length, urban textures can exhibit very different thermal characteristics compared to semi-rural or suburban areas. Moreover, it is important to highlight the meteorological conditions in which extreme temperatures can occur. During heat waves, a persistent high-pressure system traps air masses, preventing cooler air from moving in and creates air stagnation close to the ground. This leads to elevated temperatures and low wind speeds. Conversely, extreme low temperatures can occur due to advection of cold air, particularly from the Arctic region or

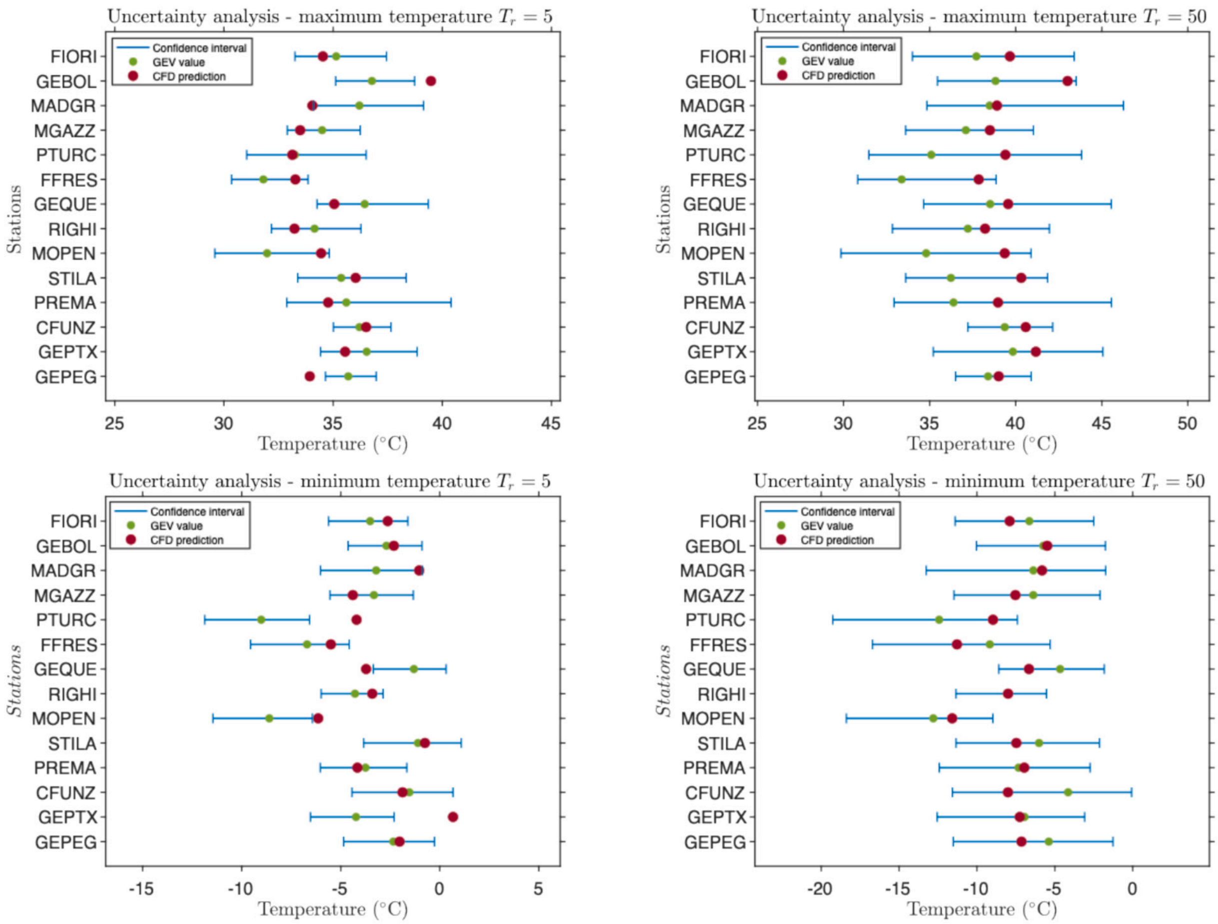


**Fig. 11.** Comparison of CFD-simulated temperatures at meteorological stations with target extreme values. Error bars represent the 95% confidence interval of the target values.

Scandinavia, causing a sudden temperature reduction that can generate downslope winds, a phenomenon typical of Liguria region (Burlando et al., 2017).

Examining the maps of extreme maximum temperature, the highest values are observed in the central part of the domain. Particularly for the 5-year return period, the temperatures range from 35 °C to 40 °C in the urban area, gradually decreasing with altitude increase toward the surrounding hills. For the 50-year return period scenario, most areas exceed a temperature of 40 °C, with localized peaks in the central valley coincident with industrial areas. In contrast, the maps of extreme minimum temperature show the lowest temperatures occur at the highest altitudes, without notably colder spots in the urban area.

### 4.2. Model validation and uncertainty analysis

The simulation results were extracted at the coordinates corresponding to the meteorological stations and compared with the values obtained from the extreme value analyses.

Determining an admissible error threshold for this study was not straightforward. To quantify the agreement between simulated and observed values, the 95% confidence intervals derived from the Generalized Extreme Value (GEV) distribution, described previously in Section 2.2, were used as reference bounds. This approach allows the evaluation of whether the simulated temperatures fall within the expected statistical range of variability for each return period, thereby providing a more rigorous assessment of model performance relative to the target values obtained from the GEV analysis. The results of this analysis for all the stations are shown in Fig. 11.

The values estimated from the CFD simulations (red dots) show good agreement with the target values (green dots) and lie within the confidence intervals across almost all stations. For the 5-year return period, summer-condition (maximum temperature) simulation (Fig. 10a), only two stations, namely GEPEG and GEBOL, display deviations, and fall slightly outside the confidence interval range. Similarly, for the 5-year return period, winter-condition (minimum temperature) simulation, GEPTX and PTURC fall slightly outside the confidence intervals. This can be due to the fact that downslope winds, which are typically associated with cold outbreaks, are not fully captured in the winter-condition simulation: the consequent underestimation of cold advection determines an overestimation of the temperatures at the bottom of the valleys, where the two stations (GEPTX and PTURC) are located.

This limitation of the model can also be observed from the analysis reported in Fig. 12, where the anomalous temperatures obtained for the maximum and minimum maps associated with 5-year return period are compared to the magnitude of the wind speed. Here, anomalous temperatures refer to unrealistic and physically implausible values occurring in certain areas characterized by complex topography, where wind speed decreases drastically. A negative relationship between the wind speed and the temperature is observed, reinforcing the idea that higher and anomalous temperatures are associated with local stagnation. The stagnation points are found along the valley floors and at foothills where the terrain flattens. Specifically, Fig. 13 illustrates these localized effects by plotting the temperature against the altitude, the slope inclination and the terrain concavity. In the present context, inclination refers to the local terrain slope angle relative to the horizontal plane, while concavity describes the local curvature of the terrain, indicating whether the surface is locally concave or convex based on the second derivative of elevation. Overall, temperature decreases with altitude although some increases occur locally along the valleys. Inclination and concavity, both centered around zero, highlight that the majority of anomalous temperatures is found on flat land.

Despite these discrepancies and considering that none of the target values are used to force the simulation, the results demonstrate the general model's ability to properly reproduce the main physical and meteorological conditions responsible of extreme high/low temperature conditions in this area.

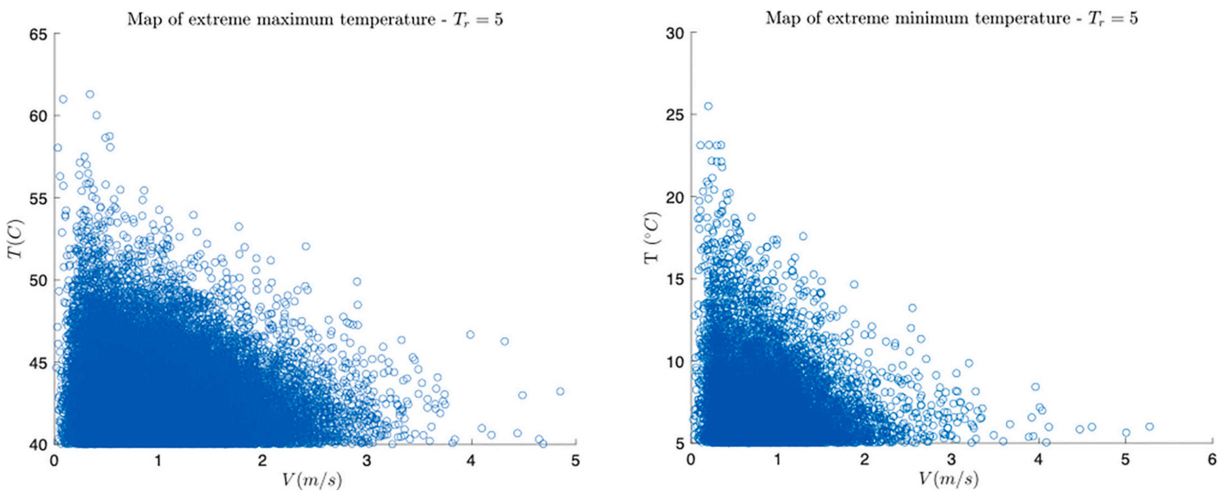


**Fig. 12.** Comparison between the 5-year return period maximum and minimum anomalous temperatures and the wind speed.

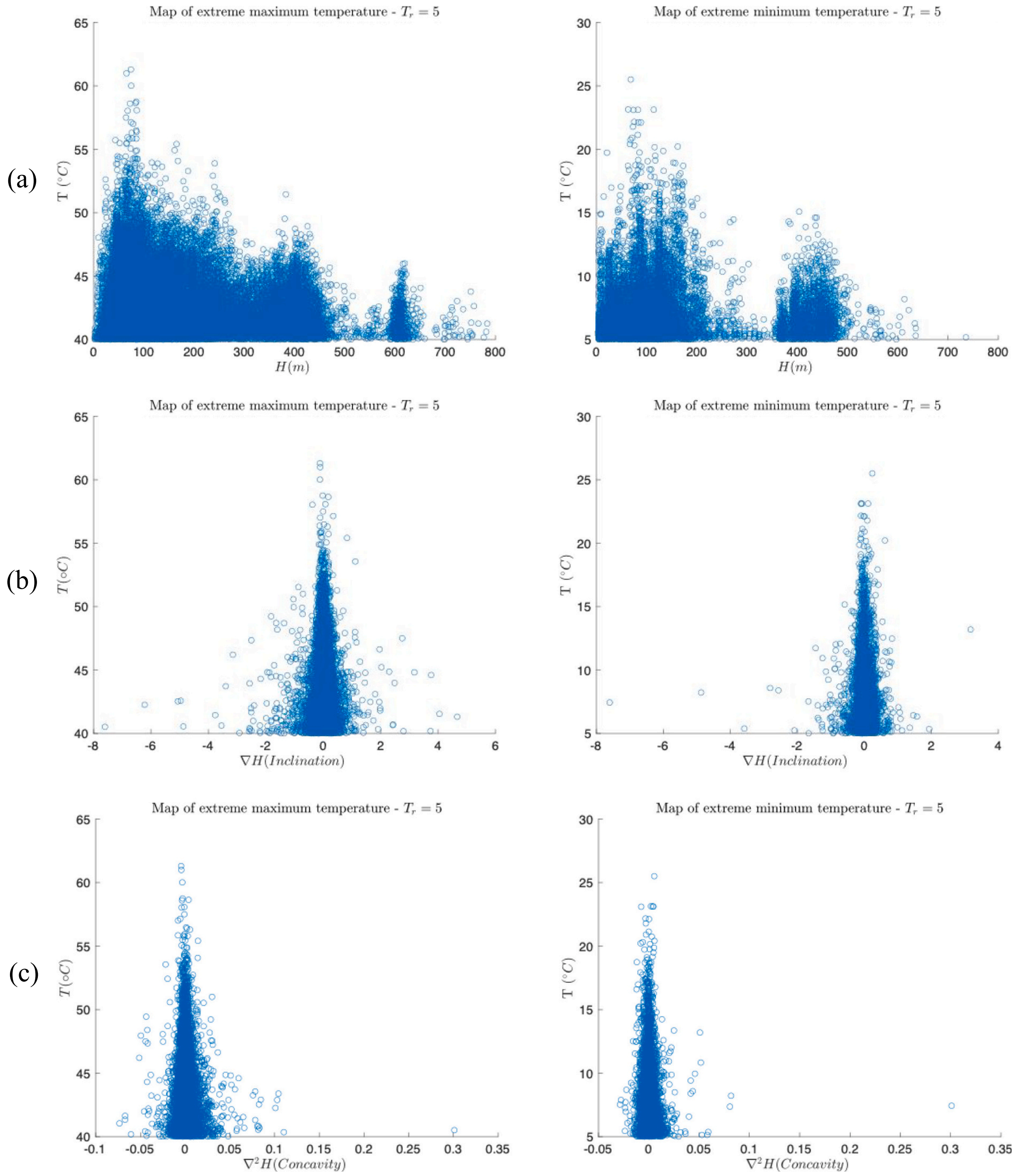


**Fig. 13.** Comparison between the 5-year return period maximum and minimum anomalous temperatures and the characteristics of the local orography as measured by the altitude (a), the inclination (b) and concavity (c).

### *4.3. UHI circulation*

The UHI effect has been predominantly studied in inland cities, where it is generally considered most critical. However, as shown by Masson et al. (2025) the UHI phenomenon is also relevant for coastal cities, particularly during the daytime. In these areas, the central part of the city facing the sea experiences a slight UHI effect due to the moderating influence of the sea breeze. Conversely, the inner parts of the city, shielded from the sea breeze, tend to exhibit moderate UHI intensity. As illustrated in Fig. 10 of Section 4.1, the internal areas show higher temperature values indeed.

In the complex context of the city of Genoa, it is essential to consider the whole topographic morphology to properly analyze the UHI effect: the city develops along a narrow strip between the sea and the surrounding mountains, with certain extensions stretching toward the internal valleys. In Fig. 14, three different sections have been extracted from the domain from the maximum 50-year return period temperature to analyze if the typical dynamics of the urban Heat Island Circulation (HIC) are captured by the simulations. Section A-A' is along the middle of the city, while section B-B′ and C-C′ are along the east side and the west side, respectively, where the city is predominant on the coast only and a major part of the section represents rural areas.

Observing section A–A′ in Fig. 14, it is possible to identify the urban HIC similar to the one found and defined by Yoshikado (1992) which is a typical feature of the UHI effect. This circulation is characterized by ground convergence near the urban center, followed by a central updraft and a divergence at higher altitude that is consistent with the findings in the literature (e.g. Cenedese and Monti, 2003; Hu et al., 2022; Wang et al., 2025). At the edges of the circulation, downdrafts are observed. The horizontal and vertical velocity components at 400 m ASL, extracted along section A-A', are reported in Fig. 15 and reinforce the aforementioned trend. The velocity vectors indicate that the interaction with the lateral boundaries is minimal and can therefore be considered negligible, supporting the use of a closed computational domain for this study.

Another important yet often overlooked aspect concerns the influence of topography and complex terrain on UHI circulation. While most studies focus on idealized or simplified scenarios, only a few address pseudo-realistic cases (Mei et al., 2025; Yu et al., 2025). Indeed, the flow patterns from section A-A' suggest that the circulation mechanisms observed in the idealized cases appear consistent with those carried out over complex topography. In section B–B′, the updraft appears slightly inclined and the convergence is enhanced due to topographic effects induced by the presence of a mountain located in front of the sea. On contrary in section C-C′, where mostly rural area is present, it is possible to observe a very low and almost negligible updraft and convection. This confirms that, in a situation of low background wind speed (i.e., the one induced by the larger scale pressure field), the primary circulation of the city experiencing the UHI phenomena is led by the convection occurring in the central part of the city.

A similar situation can also be found during the wintertime, when it is possible to experience the extreme minimum temperature. Section D-D′ (Fig. 16), extracted from minimum 50-year return period temperature, shows a similar pattern to Fig. 14, with the presence of an updraft close to the city center, even if lower in magnitude, that generates the UHI circulation. Furthermore, several secondary closed circulations are also observed, due to the interaction between the warmer sea and the cooler ground.

## 5. Limitations and perspectives

While the proposed methodology successfully integrates extreme value analysis with CFD simulations to produce high-resolution temperature maps, certain limitations remain. The representation of urban and rural land cover, for example, relies on the CORINE dataset, which categorizes areas broadly and may not fully capture finer-scale heterogeneity such as small green spaces, impervious

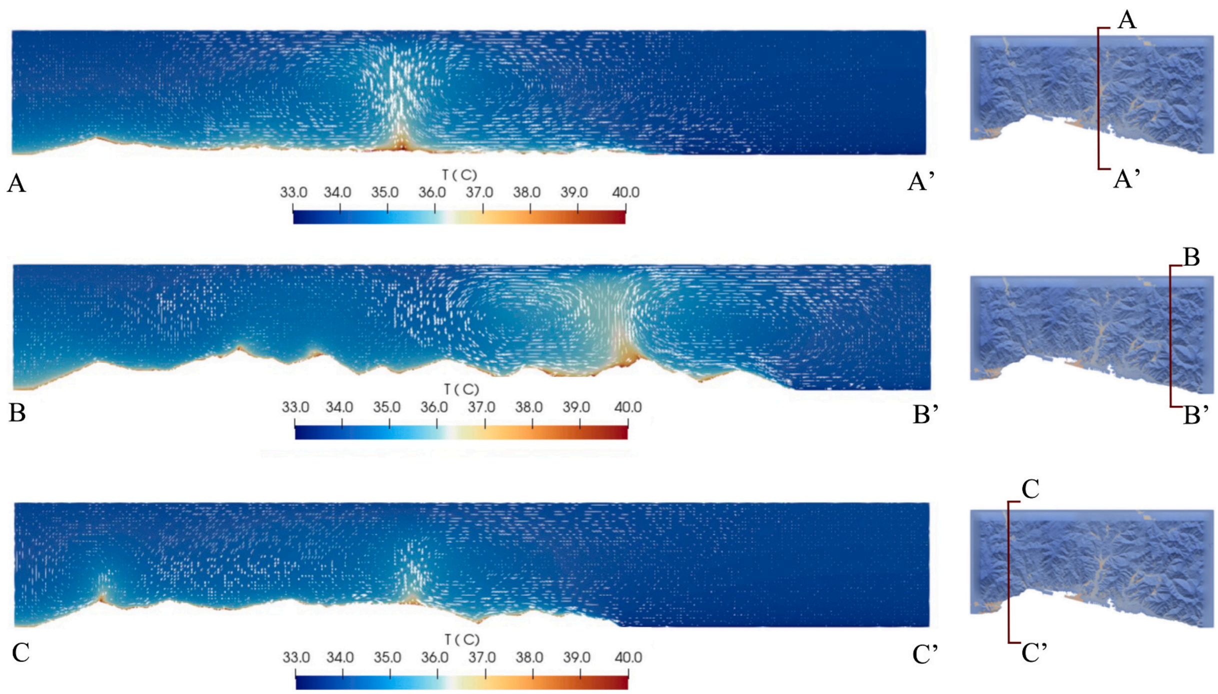


**Fig. 14.** Temperature contours overlaid with velocity vectors illustrating the development and spatial structure of urban Heat Island Circulation (HIC) in three representative areas of the city for the 50-year return period maximum temperature scenario.

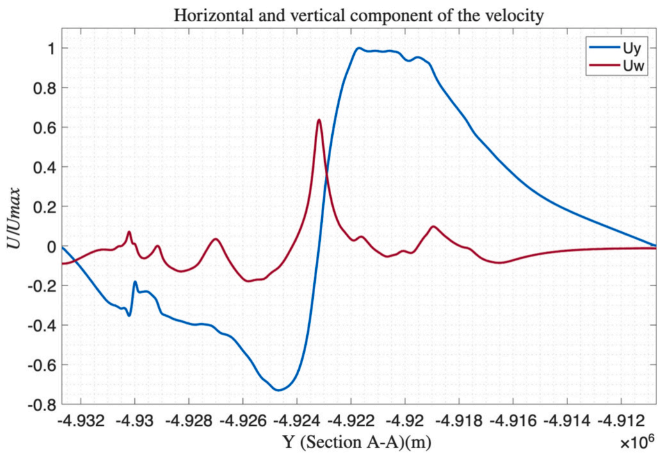


**Fig. 15.** Horizontal and vertical velocity profile extracted along the Y-axis at 400 m ASL (cross-section A-A').

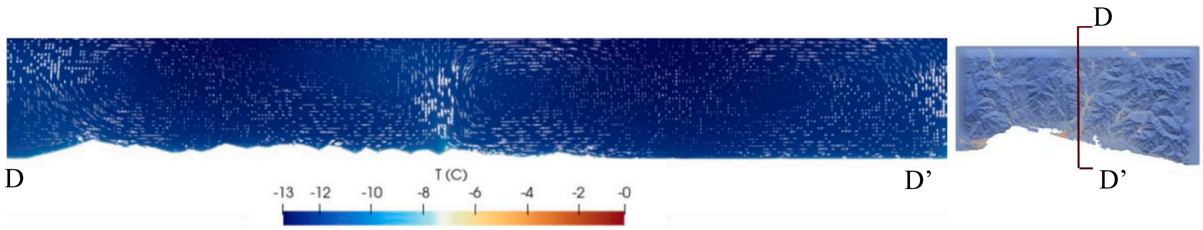


**Fig. 16.** Velocity vector field superimposed over temperature contours (left) showing the urban HIC along the D-D′ section of the city (right) for the 50-year return period minimum temperature simulation.

surfaces, or variations in building density. Additionally, the current simulations assume steady-state conditions and do not explicitly model transient phenomena such as cold-air advection or downslope winds, which may affect locally the extreme minimum temperature distribution. Future research could focus on refining the land cover characterization to better account for small-scale variations and surface properties, potentially incorporating high-resolution satellite imagery or local urban morphology data. Incorporating transient simulations using more sophisticated but computationally demanding techniques like URANS or LES could also help capture short-term atmospheric phenomena and improve the fidelity of extreme temperature predictions. However, the computational feasibility of such an effort should first be assessed. The model performance could further be enhanced by incorporating additional physical processes, such as long-wave and short-wave radiative exchange, which play an important role in urban energy balance. Overall, these improvements would enhance the accuracy of urban extreme temperature maps and further support evidence-based strategies for urban planning, heat mitigation, and public health interventions.

## 6. Conclusions

The extreme maximum and minimum temperature maps for the Municipality of Genoa for return periods of 5 and 50 years have been estimated using CFD simulations and validated by comparison against values derived from extreme value analysis of field measurements. Measurements from several meteorological stations with over 20 years of continuous recordings were collected to perform the analysis and estimate the temperatures associated with different return periods for each station. Extreme value analysis was performed using GEV, and confidence intervals were used to estimate the uncertainty of this approach. An accurate topographic model of the city of Genoa was developed, implicitly modeling surface roughness (z0) through the application of land cover patches from the CORINE Land Cover dataset. Four different CFD simulations were carried out by applying various temperature lapse rates and heat fluxes. This approach allows to obtain maps of extreme, maximum and minimum, temperatures integrating the data from the meteorological stations with a mesoscale-CFD model. These maps can play a crucial role in decision-making and management at urban scale, providing means to develop evidence-based targeted mitigation strategies. The main conclusions from this study are presented below:

- The probability distribution of daily maximum and minimum temperatures throughout the year presents two peaks, reflecting seasonal variation. When considering only the summer months (Jun-Sep) for high temperatures or the winter months (Nov-Feb) for low temperatures, the data approaches a Gaussian distribution.
- The GEV distribution shows a good fit to Gumbel and Weibull distributions for all the stations.

- The application of the CORINE land cover patches allows to implicitly consider the roughness and the thermal characteristics of the surface based on different land cover types, enabling the application of CFD with a good spatial resolution at mesoscale.
- Some of the limitation of the application of the CORINE patches are mainly related to the difficulties in characterizing and subdividing more areas in the same land cover.
- Temperatures within urban areas are higher than in rural zones. However, the spatial distribution of temperature is highly affected by the topography that can locally lead to the generation of hot spots, leading to localized thermal discomfort.
- The findings of this study show a good agreement with the values estimated from the extreme value analysis for all the cases presented. However, for the extreme minimum maps the model could not fully capture the physics, because of the underestimation of some downslope winds in the real environment that affect the stations at the bottom of the valleys where simulated temperature exceeds the station-observed value.
- The proposed CFD set up is also capable of capturing Urban Heat Island (UHI) effects. A typical urban Heat Island Circulation (HIC) is observed, originating from the city center, where temperatures are higher than those of the surrounding rural areas, in agreement with previous studies.

## CRediT authorship contribution statement

**Maria Pia Repetto:** Writing – review & editing, Supervision. **Alessia Piazza:** Writing – original draft, Validation, Software, Methodology, Formal analysis, Data curation. **Girma T. Bitsuamlak:** Writing – review & editing, Supervision. **Josip Žužul:** Writing – review & editing, Resources. **Massimiliano Burlando:** Writing – review & editing, Supervision, Project administration, Funding acquisition, Conceptualization.

## Declaration of competing interest

The authors declare that they have no known competing financial interests or personal relationships that could have appeared to influence the work reported in this paper.

## Acknowledgements

This study was funded by ADAPTNOW Project "ADAPTation Capacity Strengthening for Highly Affected and Exposed Territories in the Alps NOW" (Grant No. ASP0100048). ADAPTNOW is co-financed by the European Regional Development Fund through the Interreg Alpine Space program. The authors also acknowledge the support of the Municipality of Genoa (Italy) in providing the relevant datasets used in the framework of this research study. We also acknowledge the computational resources provided by Digital Research Alliance of Canada and technical support through SHARCNET.

## Data availability

Data will be made available on request.

## References

Aksu, H., 2021. Extreme temperature return level mapping for Northwest Turkey. Theor. Appl. Climatol. 146, 1501–1512. https://doi.org/10.1007/s00704-021-03812-9.

Allegrini, J., Dorer, V., Carmeliet, J., 2015. Influence of morphologies on the microclimate in urban neighbourhoods. J. Wind Eng. Ind. Aerodyn. 144, 108–117. https://doi.org/10.1016/j.jweia.2015.03.024.

Andriambololonaharisoamalala, R.R., Helmholz, P., Bulatov, D., Ivanova, I., Song, Y., Soon, S., Jones, E., 2025. Downscaling of urban land surface temperatures using geospatial machine learning with Landsat 8/9 and Sentinel-2 imagery. Remote Sens. 17. https://doi.org/10.3390/rs17142392.

Auld, G., Hegerl, G.C., Papastathopoulos, I., 2023. Changes in the distribution of annual maximum temperatures in Europe. Adv. Stat. Climatol. Meteorol. Oceanogr. 9, 45–66. https://doi.org/10.5194/ascmo-9-45-2023.

Bouyer, J., Inard, C., Musy, M., 2011. Microclimatic coupling as a solution to improve building energy simulation in an urban context. Energ. Buildings 43, 1549–1559. https://doi.org/10.1016/j.enbuild.2011.02.010.

Burlando, M., Tizzi, M., Solari, G., 2017. Characteristics of downslope winds in the Liguria region. Wind Struct. 24, 613–635. https://doi.org/10.12989/was.2017.24.6.613.

Buzzi, A., Davolio, S., Malguzzi, P., Drofa, O., Mastrangelo, D., 2014. Heavy rainfall episodes over Liguria in autumn 2011: numerical forecasting experiments. Nat. Hazards Earth Syst. Sci. 14, 1325–1340. https://doi.org/10.5194/nhess-14-1325-2014.

Cassola, F., Ferrari, F., Mazzino, A., Miglietta, M.M., 2016. The role of the sea on the flash floods events over Liguria (northwestern Italy). Geophys. Res. Lett. 43, 3534–3542. https://doi.org/10.1002/2016GL068265.

Cenedese, A., Monti, P., 2003. Interaction between an inland urban Heat Island and a sea-breeze flow: a laboratory study. Am. Meteorol. Soc. 42, 1569–1583.

Davenport, A.G., 1961. A Statistical Approach to the Treatment of Wind Loading on Tall Masts and Suspension Bridges. University of Bristol, Bristol.

De Quadros, B.M., Pigliautile, I., Pisello, A.L., Krüger, E., Mizgier, M.O., 2024. Reliability of urban microclimate simulations: spatio-temporal validation through intra-urban canyon transects for outdoor thermal comfort analysis. Int. J. Biometeorol. 68, 2715–2729. https://doi.org/10.1007/s00484-024-02784-5.

Founda, D., Santamouris, M., 2017. Synergies between urban Heat Island and heat waves in Athens (Greece), during an extremely hot summer (2012). Sci. Rep. 7. https://doi.org/10.1038/s41598-017-11407-6.

Garcia-Herrera, R., Díaz, J., Trigo, R.M., Luterbacher, J., Fischer, E.M., 2010. A review of the European summer heat wave of 2003. Crit. Rev. Environ. Sci. Technol. https://doi.org/10.1080/10643380802238137.

Giannaros, T.M., Melas, D., 2012. Study of the urban heat island in a coastal Mediterranean City: the case study of Thessaloniki. Greece. Atmos. Res. 118, 103–120. https://doi.org/10.1016/j.atmosres.2012.06.006.

Gohain, K.J., Goswami, A., Mohammad, P., Kumar, S., 2023. Modelling relationship between land use land cover changes, land surface temperature and urban heat island in Indore city of Central India. Theor. Appl. Climatol. 151, 1981–2000. https://doi.org/10.1007/s00704-023-04371-x.

Hargreaves, D.M., Wright, N.G., 2007. On the use of the k-ε model in commercial CFD software to model the neutral atmospheric boundary layer. Journal of Wind Engineering and Industrial Aerodynamics 95, 355–369. https://doi.org/10.1016/j.jweia.2006.08.002.

Holmes, J.D., 2007. Wind Loading on Structures, Second edition. Spon Press, New York.

Hu, Y., Tan, J., Grimmond, S., Ao, X., Yan, Y., Liu, D., 2022. Observed and modeled urban Heat Island and sea-breeze circulation interactions: a Shanghai case study. J. Appl. Meteorol. Climatol. 61, 239–259. https://doi.org/10.1175/JAMC-D-20-0246.1.

IPCC, 2023. Climate Change 2023: Synthesis Report. Contribution of Working Groups I, II and III to the Sixth Assessment Reportof the Intergovernmental Panel on Climate Change [Core Writing Team. IPCC, Geneva. https://doi.org/10.59327/IPCC/AR6-9789291691647.

Ivajnšič, D., Žiberna, I., 2019. The effect of weather patterns on winter small city urban heat islands. Meteorological Applications 26, 195–203. https://doi.org/10.1002/met.1752.

Kadakia, K.T., Galea, S., 2023. Urbanization and the future of population health. Milbank Q 101, 153–175. https://doi.org/10.1111/1468-0009.12624.

Kassomenos, P.A., Katsoulis, B.D., 2006. Mesoscale and macroscale aspects of the morning urban Heat Island around Athens, Greece. Meteorol. Atmos. Phys. 94, 209–218. https://doi.org/10.1007/s00703-006-0191-x.

Kim, Y.-H., Baik, J.-J., 2005. Spatial and Temporal Structure of the Urban Heat Island in Seoul.

Kim, G., Lee, G., 2024. Validation of CFD models of urban microclimates under high temperature and humidity conditions during daytime heatwaves in dense low-rise areas. Build. Environ. 266. https://doi.org/10.1016/j.buildenv.2024.112087.

Kong, J., Zhao, Y., Carmeliet, J., Lei, C., 2021. Urban heat island and its interaction with heatwaves: a review of studies on mesoscale. Sustainability (Switzerland) 13. https://doi.org/10.3390/su131910923.

Korah, A., Wimberly, M.C., 2024. Annual impervious surface data from 2001–2020 for west African countries: Ghana, Togo, Benin and Nigeria. Sci. Data 11. https://doi.org/10.1038/s41597-024-03610-8.

Korah, A., Smith, L.C., Wimberly, M.C., 2025. Understanding urban expansion across primary and secondary cities in Ghana. Habitat Int. 158. https://doi.org/10.1016/j.habitatint.2025.103339.

Laino, E., Iglesias, G., 2023. Extreme climate change hazards and impacts on European coastal cities: a review. Renew. Sustain. Energy Rev. https://doi.org/10.1016/j.rser.2023.113587.

Luna, M.Y., Morata, A., Almarza, C., Martín, M.L., 2006. The use of GIS to evaluate and map extreme maximum and minimum temperatures in Spain. Meteorol. Appl. 13, 385–392. https://doi.org/10.1017/S1350482706002386.

Masselot, P., Mistry, M.N., Rao, S., Huber, V., Monteiro, A., Samoli, E., Stafoggia, M., de'Donato, F., Garcia-Leon, D., Ciscar, J.C., Feyen, L., Schneider, A., Katsouyanni, K., Vicedo-Cabrera, A.M., Aunan, K., Gasparrini, A., 2025. Estimating future heat-related and cold-related mortality under climate change, demographic and adaptation scenarios in 854 European cities. Nat. Med. 31, 1294–1302. https://doi.org/10.1038/s41591-024-03452-2.

Masson, V., Lemonsu, A., Hidalgo, J., Voogt, J., 2025. Annual Review of Environment and Resources Urban Climates and Climate Change, 58, p. 46. https://doi.org/10.1146/annurev-environ-012320.

Mei, S.J., Hang, J., Fan, Y., Yuan, C., Xue, Y., 2025. CFD simulations on the wind and thermal environment in urban areas with complex terrain under calm conditions. Sustain. Cities Soc. 118. https://doi.org/10.1016/j.scs.2024.106022.

Mestayer, P.G., Durand, P., et al., 2005. The urban boundary-layer field campaign in Marseille (UBL/CLU-ESCOMPTE): set-up and first results. Bound.-Lay. Meteorol. 114. https://doi.org/10.1007/s10546-004-9241-4ï.

Milner, J., Harpham, C., Taylor, J., Davies, M., Le Quéré, C., Haines, A., Wilkinson, P., 2017. The challenge of urban heat exposure under climate change: an analysis of cities in the sustainable healthy urban environments (SHUE) database. Climate 5. https://doi.org/10.3390/cli5040093.

Mirzaei, P.A., Haghighat, F., 2010. Approaches to study urban Heat Island - abilities and limitations. Build. Environ. 45, 2192–2201. https://doi.org/10.1016/j.buildenv.2010.04.001.

Mitchell, D., Heaviside, C., Vardoulakis, S., Huntingford, C., Masato, G., P Guillod, B., Frumhoff, P., Bowery, A., Wallom, D., Allen, M., 2016. Attributing human mortality during extreme heat waves to anthropogenic climate change. Environ. Res. Lett. 11. https://doi.org/10.1088/1748-9326/11/7/074006.

Oke, T.R., 1982. The energetic basis of the urban heat island. Quart. J. R. Met. Soc. 108, 1–24. https://doi.org/10.1002/qj.49710845502.

Pigliautile, I., Pisello, A.L., 2018. A new wearable monitoring system for investigating pedestrians' environmental conditions: development of the experimental tool and start-up findings. Sci. Total Environ. 630, 690–706. https://doi.org/10.1016/j.scitotenv.2018.02.208.

Pongracz, R., Bartholy, J., Dezso, Z., 2006. Remotely sensed thermal information applied to urban climate analysis. Adv. Space Res. 37, 2191–2196. https://doi.org/10.1016/j.asr.2005.06.069.

Ricci, A., Burlando, M., 2025. Implementing surface roughness in OpenFOAM using the CORINE database for mesoscale CFD simulations, in: proceedings of the 9th European African conference on wind engineering. Trondheim, pp. 841–844.

Richards, P.J., Hoxey, R.P., 1993. Appropriate boundary conditions for computational wind engineering models using the k-E turbulence model. J. Wind Eng. Ind. Aerodyn. 46-47, 145–153. https://doi.org/10.1016/0167-6105(93)90124-7.

Ritchie, H., Samborska, V., Roser, M., 2018. Urbanization [WWW document]. Visited in December, 2025.

Romero Rodríguez, L., Sánchez Ramos, J., Sánchez de la Flor, F.J., Álvarez Domínguez, S., 2020. Analyzing the urban heat island: comprehensive methodology for data gathering and optimal design of mobile transects. Sustain. Cities Soc. 55. https://doi.org/10.1016/j.scs.2020.102027.

Russo, S., Sillmann, J., Fischer, E.M., 2015. Top ten European heatwaves since 1950 and their occurrence in the coming decades. Environ. Res. Lett. 10. https://doi.org/10.1088/1748-9326/10/12/124003.

Santiago, J.L., Krayenhoff, E.S., Martilli, A., 2014. Flow simulations for simplified urban configurations with microscale distributions of surface thermal forcing. Urban Clim. 9, 115–133. https://doi.org/10.1016/j.uclim.2014.07.008.

Schielicke, L., Pfahl, S., 2022. European heatwaves in present and future climate simulations: a Lagrangian analysis. Weather and Climate Dynamics 3, 1439–1459. https://doi.org/10.5194/wcd-3-1439-2022.

Stewart, I.D., Oke, T.R., 2012. Local climate zones for urban temperature studies. Bull. Am. Meteorol. Soc. 93, 1879–1900. https://doi.org/10.1175/BAMS-D-11-00019.1.

Thompson, V., Mitchell, D., Hegerl, G.C., Collins, M., Leach, N.J., Slingo, J.M., 2023. The most at-risk regions in the world for high-impact heatwaves. Nat. Commun. 14. https://doi.org/10.1038/s41467-023-37554-1.

Tominaga, Y., Mochida, A., Yoshie, R., Kataoka, H., Nozu, T., Yoshikawa, M., Shirasawa, T., 2008. AIJ guidelines for practical applications of CFD to pedestrian wind environment around buildings. Journal of Wind Engineering and Industrial Aerodynamics 96, 1749–1761. https://doi.org/10.1016/j.jweia.2008.02.058.

Toparlar, Y., Blocken, B., Vos, P., Van Heijst, G.J.F., Janssen, W.D., van Hooff, T., Montazeri, H., Timmermans, H.J.P., 2015. CFD simulation and validation of urban microclimate: a case study for Bergpolder Zuid, Rotterdam. Build. Environ. 83, 79–90. https://doi.org/10.1016/j.buildenv.2014.08.004.

Unger, J., 1996. Heat island intensity with different meteorological conditions in a medium-sized town: Szeged, Hungary. Theor. Appl. Climatol. https://doi.org/10.1007/BF00865157.

Voogt, J.A., Oke, T.R., 2003. Thermal remote sensing of urban climates. Remote Sens. Environ. 86, 370–384. https://doi.org/10.1016/S0034-4257(03)00079-8.

Wang, Y., Wang, Jing, Yu, Z., Wu, S., Wang, Jukun, Wang, X., 2025. Evolution of urban heat island circulation for the flat city. Energy Built Environ. https://doi.org/10.1016/j.enbenv.2025.02.004.

Wieringa, J., 1992. Updating the Davenport roughness classification. J. Wind Eng. Ind. Aerodyn. 357–368. https://doi.org/10.1016/0167-6105(92)90434-C.

Wyatt, B., Briggs, D., Mounsey, H., 1988. CORINE: An information system on the state of the environment in the European Community. In: Mounsey, H., Tomlinson, R. (Eds.), Building Databases for Global Science. Taylor & Francis, London, pp. 378–396.

Yao, R., Wang, L., Huang, X., Cao, Q., Peng, Y., 2022. A method for improving the estimation of extreme air temperature by satellite. Sci. Total Environ. 837. https://doi.org/10.1016/j.scitotenv.2022.155887.

Yoshikado, A., 1992. Numerical study of the daytime urban effect and its interaction with the sea breeze. American Meteorological Society 31, 1146–1164. https://doi.org/10.1175/1520-0450(1992)031<1146:NSOTDU>2.0.CO;2.

Yu, Z., Wang, Y., Wang, J., Wang, X., Wu, S., 2025. Evolution characteristics of urban Heat Island circulation for loess Tableland Valley towns. Buildings 15. https://doi.org/10.3390/buildings15152649.

Žužul, J., Ricci, A., Burlando, M., 2025. An automated geometry generation procedure for CWE applications in OpenFOAM: the case study of a thunderstorm downburst moving over Genoa city. Meccanica 60, 1753–1770. https://doi.org/10.1007/s11012-024-01816-z.